RSC Advances

PAPER

View Article Online
View Journal | View Issue

Check for updates

Cite this: *RSC Adv.*, 2024, **14**, 13685

Preparation of cyclodextrin polymer-functionalized polyaniline/MXene composites for high-performance supercapacitor†

Tingting He,[a] Xusen Li,[a] Bingxin Sun,[a] Liwei Lin,[bc] Fang Guo,*[d] Guowang Diao,[a] Yuanzhe Piao[ce] and Wang Zhang*[acf]

Controlled aggregation is of great significance in designing nanodevices with high electrochemical performance. In this study, an *in situ* aggregation strategy with cyclodextrin polymer (CDP) was employed to prepare polyaniline (PANI)/MXene (MX) composites. MXene served as a two-dimensional structure template. Due to supramolecular interactions, CDP could be controllably modified with PANI layers, effectively preventing the self-polymerization of PANI. As a result, this integration facilitated a more uniform growth of PANI on MXene and further improved the capacitance performance of CDP-MX/PA. In a three-electrode system, the specific capacitance of MX/PA at 1 A g^{-1} was 460.8 F g^{-1}, which increased to 523.8 F g^{-1} after CDP-induced growth. CDP-MX/PA exhibited a high energy density of 27.7 W h kg^{-1} at a power density of 700 W kg^{-1}. This suggests that the synthetic strategy employed in this study holds promise in providing robust support for the preparation of high-performance energy-storage device.

Received 4th April 2024
Accepted 21st April 2024

DOI: 10.1039/d4ra02542c

rsc.li/rsc-advances

Open Access Article. Published on 25 April 2024. Downloaded on 2/12/2026 9:24:58 AM.
This article is licensed under a Creative Commons Attribution-NonCommercial 3.0 Unported Licence.

1 Introduction

Supercapacitors, also referred to as electrochemical capacitors, represent advanced electronic storage devices distinguished by their remarkable capacity, high power density, and extended cycle life.[1–4] MXene, a notable two-dimensional material, stands out as a highly promising candidate for supercapacitor applications. Its exceptional conductivity lays a solid foundation for accelerating charge transfer rates and augmenting the power density of supercapacitors.[5–7] This is primarily due to MXene's remarkable electrical conductivity and the abundance of surface functional groups, enabling effective integration with other materials to enhance the performance of electrode materials.[8,9] Furthermore, a high specific surface area of MXene also plays a vital role in expanding the contact interface between the electrode and electrolyte, thereby elevating energy density.

Polyaniline (PANi), known for its impressive electrochemical properties, plays a pivotal role in improving the charge transfer efficiency of supercapacitors, thus achieving higher power density.[10,11] PANi also exhibits commendable capacitance performance, further enhancing the overall capacitance of the capacitor. Its inherent chemical reactivity positions it as an ideal electrode material, capable of effectively hosting charges and enhancing the energy density of the capacitor. Nonetheless, the volume expansion issue that arises when MXene is employed in supercapacitors may result in structural damage to electrode materials, consequently affecting the cycle life. PANi's high conductivity bolsters the charge transfer rate, while PANi's electrochemical activity provides additional charge storage sites, collectively propelling both energy density and power density of the capacitor.[12,13]

The special molecular structure of cyclodextrin polymer (CDP) introduces additional host–guest recognition ability, thereby enhancing the interaction between the electrode material and the capacitor's electrolyte. This heightened interfacial effect is anticipated to elevate the overall electrochemical performance.[14–16] Additionally, the molecular recognition ability of CDP may influence electrode material selection and electrolyte permeability within the capacitor through interactions with MXene and PANi. This molecular recognition property can regulate the capacitor's surface chemical characteristics, enhancing the specific attributes of the electrode material and optimizing the capacitor's overall performance.[17–19]

[a]*School of Chemistry and Chemical Engineering, Yangzhou University, Yangzhou, Jiangsu, 225009, P. R. China. E-mail: zhangwang@yzu.edu.cn; zhangwang@snu.ac.kr*
[b]*School of Petrochemical Engineering, Changzhou University, Changzhou, Jiangsu, 213164, P. R. China*
[c]*Department of Applied Bioengineering, Graduate School of Convergence Science and Technology, Seoul National University, Seoul, 08826, Republic of Korea*
[d]*School of Chemistry and Chemical Engineering, Yancheng Institute of Technology, Yancheng, Jiangsu, 224051, P. R. China. E-mail: gfycit@163.com*
[e]*Advanced Institutes of Convergence Technology, 145 Gwanggyo-ro, Yeongtong-gu, Suwon-si, Gyeonggi-do, 16229, Republic of Korea*
[f]*Research Institute for Convergence Science, Seoul National University, Seoul, 08826, Republic of Korea*

† Electronic supplementary information (ESI) available. See DOI: https://doi.org/10.1039/d4ra02542c

© 2024 The Author(s). Published by the Royal Society of Chemistry

Open Access Article. Published on 25 April 2024. Downloaded on 2/12/2026 9:24:58 AM. This article is licensed under a Creative Commons Attribution-NonCommercial 3.0 Unported Licence.

This study revolves around the preparation of composite materials consisting of MXene, cyclodextrin polymer, and PANi, with the primary objective of elevating the energy density and cyclic stability of supercapacitors. Through harnessing the remarkable conductivity of MXene, supramolecular induced polymerization by CDP, and the electrochemical prowess of PANi, we have conceived an innovative electrode material of CDP-MX/PA. The MXene surface modified by CDP exhibits the following advantages: (1) it enhances the protonation degree of PANI, suppressing its deprotonation issue, thereby improving the oxidation–reduction activity and reversibility of PANI; (2) it increases the conductivity and flexibility of PANI, facilitating its rapid redox reactions and buffering the corresponding expansion/contraction; (3) it provides sufficient space to accommodate a large amount of PANI, ensuring a high capacity; (4) it furnishes an adequate supply of protons, thereby supporting the continuous protonation of PANI.[20,21] Our experimental results unequivocally demonstrate the exceptional performance of this composite in supercapacitors, characterized by its impressive energy density, remarkable cyclic endurance, and rapid charge–discharge capabilities. The triumphant strategy opens up new possibilities for the advancement of high-performance supercapacitors, broadening their potential applications in crucial domains like renewable energy storage.

2 Experimental section

2.1 Raw materials

MAX (Ti_3AlC_2, 400 mesh) was purchased from Jilin Technology Co., Ltd. Hydrochloric acid and lithium fluoride were all purchased from Sinopharm Chemical Reagent Co., Ltd. Ammonium persulfate (APS) and aniline were purchased from Sigma Aldrich. CD was purchased from Shanghai McLean Biochemical Co. The purity of epichlorohydrin reagent used was analytical grade. The reagents required for the experiments in this study did not need to be purified.

2.2 Preparation of MXene

According to previous literature,[22] MXene nanosheets are prepared by selectively etching the Al layer in Ti_3AlC_2 using a mixed solution of LiF and HCl. Briefly stated, 2.0 g of LiF is weighed and dissolved in 40.0 mL of 9 M HCl. The etching solution becomes homogeneous after 15 min of stirring. Subsequently, 1.0 g of Ti_3AlC_2 is slowly added to the combination solution and stirred at 450 rpm for 24 h at 35 °C. Afterward, the solution is centrifuged at 3500 rpm, and the supernatant is discarded. Repeat this centrifugation procedure until the pH of the supernatant reaches 7. After centrifugation, the product is quickly frozen in liquid nitrogen and then placed in a freeze dryer for 48 h. The obtained product is MXene nanosheets.

2.3 Preparation of CDP

Using an analytical balance, 20.0 g of NaOH were weighed and added to 40.0 mL of deionized water for dissolution. Subsequently, the mixed solution was transferred to a 250 mL three-necked flask, and 25.0 g of β-CD was added to the solution. Mechanical stirring was used for 1 h to ensure complete dissolution of β-CD. Following this, 10.0 mL of epichlorohydrin was added, and the mixture was stirred for 12 h at room temperature. After the reaction had been completed, the precipitate was washed with deionized water, dried under vacuum, and then ground to obtain the CDP sample.[23]

2.4 Preparation of CDP-MX/PA

Disperse 80 mM of aniline monomer, 20.0 mg of MXene, and 120.0 mg of CDP in 20.0 mL of 1 M hydrochloric acid solution, and stir for 1 h at 0 °C to ensure uniform mixing of the materials. Further, add 900.0 mg of APS and 20.0 mL of 1 M HCl. Continue stirring at 0 °C for an additional 8 h. Collect the precipitate by centrifugation, and finally wash the solid precipitate three times with deionized water. The CDP-MX/PA sample can be obtained by vacuum drying. According to the concentration of aniline added, the resulting materials were named as CDP-MX/PA-40, CDP-MX/PA-60, CDP-MX/PA-80, and CDP-MX/PA-100. The schematic diagram of the preparation of CDP-MX/PA composite is shown in Scheme 1.

The synthesis method for MX/PA is identical to the one described above.

2.5 Electrochemical testing

The assembly process of the two-electrode system is as follows: the active material, acetylene black, and PVDF are dissolved in an appropriate amount of NMP in a mass ratio of 8 : 1 : 1. After stirring for 12 h, the mixture is uniformly coated onto pre-cut titanium foil discs with a radius of 0.8 cm. After drying in a vacuum oven for 12 h, the loading amount of the active substance is calculated based on the difference in mass of the electrode before and after. The loading amount of the active material in electrode is 2.0 mg. The two-electrode systems in this work all use symmetrical supercapacitors, with both positive and negative electrodes composed of the active material to

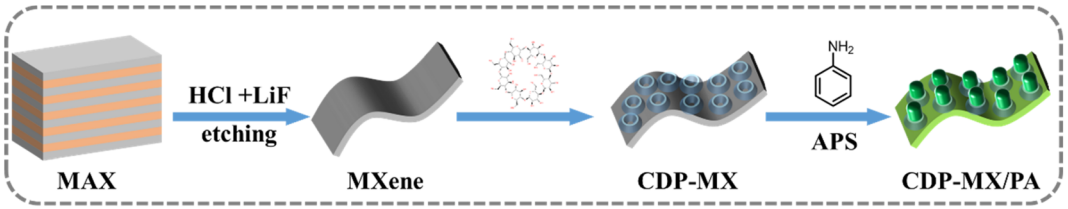

Scheme 1 Schematic of the synthesis process of CDP-MX/PA composites.

© 2024 The Author(s). Published by the Royal Society of Chemistry

Open Access Article. Published on 25 April 2024. Downloaded on 2/12/2026 9:24:58 AM. This article is licensed under a Creative Commons Attribution-NonCommercial 3.0 Unported Licence.

be tested. A filter paper with a radius of 0.8 cm is used as the separator, and 1 M H_2SO_4 serves as the electrolyte. Assembly is conducted using Swagelok equipment, followed by a 12 hour rest period to allow the electrolyte to fully infiltrate the electrode material before proceeding to two-electrode electrochemical testing.

2.6 Characterizations of structure and morphology

Transmission electron microscopy (TEM, JEM-2100) and field emission scanning electron microscopy (SEM, Zeiss Supra 55) were employed to obtain images of composite morphology. The product was analyzed using a Fourier transform infrared (FTIR) spectrometer (Cary 610/670 micro IR spectrometer). Thermogravimetric analysis (TGA) was conducted using a TG209F3 Tarsus instrument (NETZSCH, Germany) at a heating rate of 10 °C min^{-1}, with the ambient temperature raised to 900 °C under a nitrogen atmosphere. X-Ray photoelectron spectroscopy (XPS) measurements were carried out to analyze the element composition of composite materials. Electrochemical tests were conducted on an electrochemical workstation (CH Instruments, 760E). Electrochemical tests in both three-electrode and two-electrode systems are presented in the ESI.†

3 Results and discussion

3.1 Morphology analysis

The morphology of the prepared materials, including CDP-MX/PA, PANi and MXene, was observed using both SEM and TEM. SEM images of CDP-MX/PA synthesized with different aniline concentrations (40–100 mM) are shown in Fig. 1a–d. In CDP-MX/PA synthesized at various concentrations, pure PANi nanoparticles were rarely observed. They uniformly covered the surface of MXene and exhibited relatively ordered growth. Due to the excellent water solubility and supramolecular recognition ability of CDP, it provides a suitable environment for the polymerization of aniline on MXene. At 40 mM aniline concentration, small aniline nanoparticles appeared on the surface of MXene, as shown in Fig. 1a. As the aniline concentration increased to 60 mM, PANi nanowires began to emerge on the material surface (Fig. 1b). With a further increase in aniline concentration to 80 mM, PANi nanowires increased, forming a mesh-like structure (Fig. 1c and l), acting as connectors between MXene layers, facilitating ion diffusion in supercapacitors. However, when the aniline concentration reached 100 mM, significant aggregation of the material occurred (Fig. 1d), attributed to aniline oversaturation during the polymerization process.[24] The EDS image in Fig. 1e, as shown in Fig. 1f–i, demonstrates the uniform distribution of C, O, Ti, and N elements, confirming the successful growth of PANi on CDP-functionalized MXene. The structure of PANi is depicted in Fig. 1j and S1a,† showing a tubular structure with disordered stacking. In contrast, MXene consists of single-layered sheets in Fig. 1k and S1b.† SEM image of MX/PA-80 in Fig. S1c† shows that compared with CDP-MX/PA, PANi grows more disorderly on MXene. After adding APS, the abundant functional groups (such as –O and –OH) on the surface of MXene serve as nucleation sites during the polymerization process, enabling the chemical oxidative polymerization of PANi on the MXene layer.[25] The addition of aniline molecules to the system induces supramolecular interactions between the hydrophobic side of aniline monomers and the cavities of CDP. This results in the hydrophobic side of aniline being encapsulated within the cavities of CDP, with the exposed amino groups serving as nucleation centers for PANi polymerization. Upon the addition of APS, amino groups confined to the surface of CDP-modified MXene initiate polymerization, leading to the uniform deposition of PANi on the surface of MXene functionalized with CDP.[26–28] The resulting PANi covers the surface of MXene while maintaining its intact sheet-like structure. This process enables the successful integration of PANi onto the MXene surface, forming a composite material where PANi uniformly deposits on the CDP-functionalized MXene surface.

3.2 Structural analysis

The chemical structure of the original CDP, PANi, MX/PA, and CDP-MX/PA composite materials was studied through Fourier-

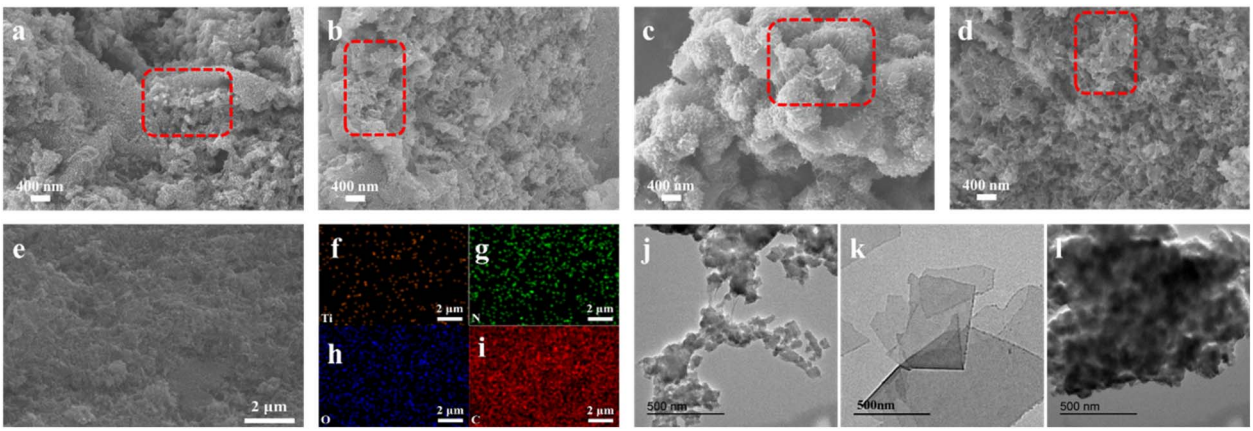

Fig. 1 SEM images of (a) CDP-MX/PA-40; (b) CDP-MX/PA-60; (c) CDP-MX/PA-80; (d) CDP-MX/PA-100; (e–i) Element mapping of CDP-MX/PA-80; TEM images of (j) PANi; (k) MXene; (l) CDP-MX/PA-80.

Open Access Article. Published on 25 April 2024. Downloaded on 2/12/2026 9:24:58 AM.
This article is licensed under a Creative Commons Attribution-NonCommercial 3.0 Unported Licence.

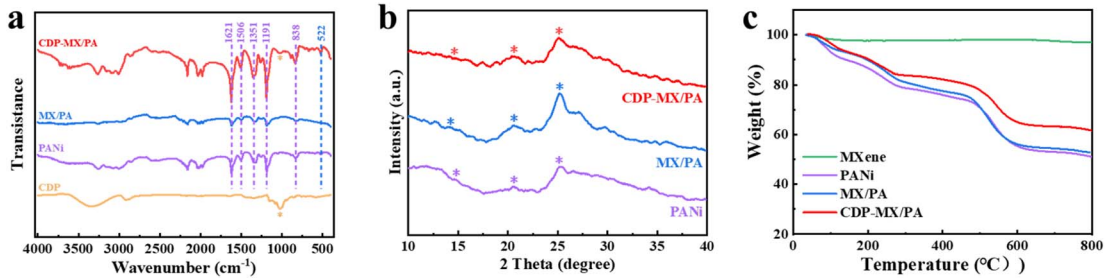

Fig. 2 (a) FTIR spectra of CDP, PANi, MX/PA, CDP-MX/PA; (b) XRD patterns of PANi, MX/PA, CDP-MX/PA; (c) TGA patterns of MXene, PANi, MX/PA, CDP-MX/PA.

transform infrared spectroscopy (FTIR), and the results are presented in Fig. 2a. The PANi peaks were observed at 1623, 1508, 1350, and 835 cm^{-1} correspond to the vibrations of –C=N, –C=C, –C–N, and –C–H, respectively.[29] The absorption peak at 603 cm^{-1} corresponds to the stretching vibration of Ti–O in MXene.[30] These characteristic peaks are also observed in MX/PA, indicating good compatibility between PANi and MXene. In addition to the mentioned absorption peaks, a characteristic peak at 1031 cm^{-1} is corresponding to the ether bond in CDP is also observed in CDP-MX/PA,[31] confirming the successful synthesis of CDP-MX/PA.

Powder X-ray diffraction (XRD) was conducted to obtain detailed structural result, and the results are depicted in Fig. 2b. The characteristic peaks observed in the XRD patterns of PANi, MX/PA, and CDP-MX/PA at $2\theta = 15.1°$, 20.6°, and 25.2° correspond to the diffraction from the (011), (020), and (200) crystal planes of PANi in its emeraldine salt form, respectively.[32] This result demonstrates that the emeraldine salt form of polyaniline is well coated on the MXene substrate, and the presence of CDP and MXene do not affect the structure of polyaniline. The presence of PANI can shield the characteristic peaks of MXene. PANI not only adheres to the surface of Ti_3C_2Tx but may also exist between its 2D layers, resulting in less distinct characteristic peaks of MXene. Fig. 2c illustrates the thermal stability of MXene, PANi, MX/PA, and CDP-MX/PA. The weight loss observed in the range of 20–100 °C for all materials is attributed

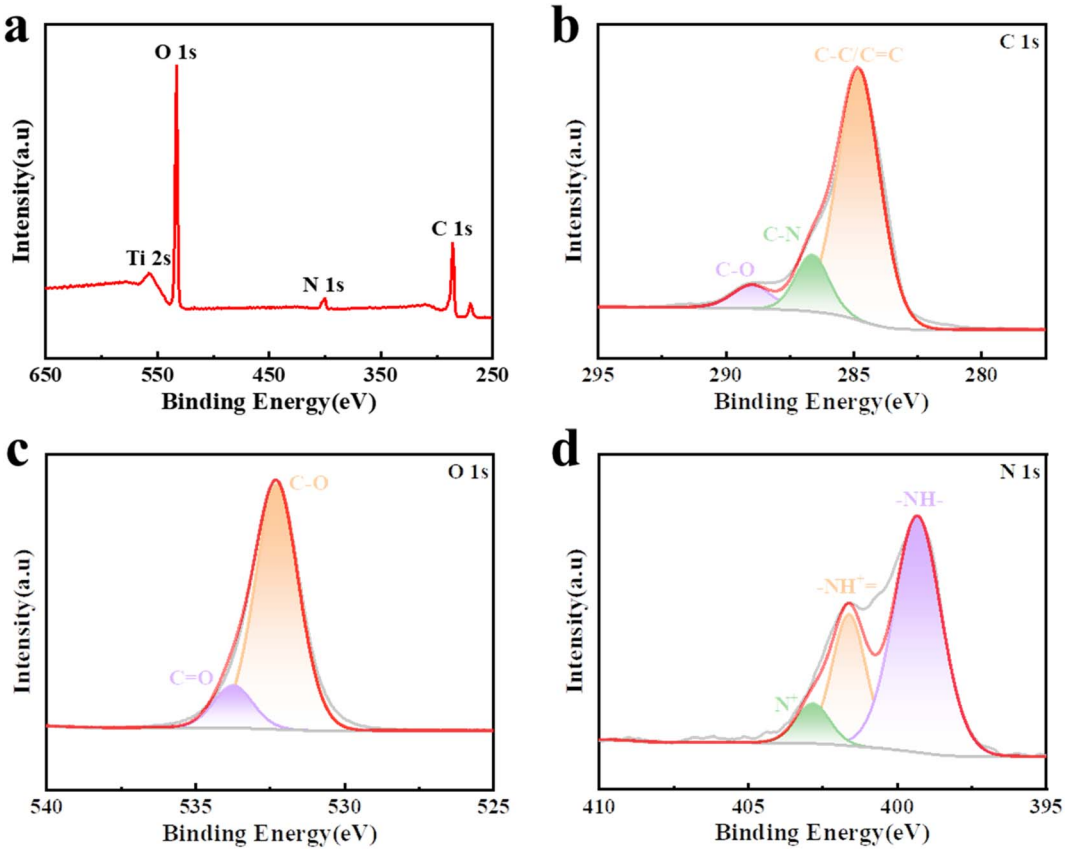

Fig. 3 (a) XPS survey spectra of CDP-MX/PA-80; (b) C 1s spectrum; (c) O 1s spectrum; and (d) N 1s spectrum.

© 2024 The Author(s). Published by the Royal Society of Chemistry

Open Access Article. Published on 25 April 2024. Downloaded on 2/12/2026 9:24:58 AM.
This article is licensed under a Creative Commons Attribution-NonCommercial 3.0 Unported Licence.

to water evaporation. For PANi, MX/PA, and CDP-MX/PA, the mass loss between 100–300 °C is primarily due to the deionization of dopants, while the loss between 400–500 °C corresponds to the thermal decomposition of the PANi main chains. Between 20–800 °C, MXene experiences minimal mass loss, with the thermal weight curve of MX/PA closely overlapping that of PANI. Therefore, the contribution of MXene to the fixed weight within this temperature range can be considered negligible. However, upon introducing CDP, the mass loss of CDP-MX/PA is 39%, which is 10% lower than that of PANI alone. This indicates that the overall thermal stability of CDP-MX/PA is superior to pure polymer. This suggests that CDP-MX/PA can mitigate size changes caused by temperature variations, thereby enhancing the operational lifespan and performance of the device.

X-Ray photoelectron spectroscopy (XPS) spectra were obtained to assess the samples' composition, as shown in Fig. 3a. The measured spectral peaks of C 1s at 286 eV, O 1s at 533 eV, and N 1s at 399 and 401.5 eV are associated with CDP-MX/PA.[33] Fig. 3b presents the C 1s spectrum of CDP-MX/PA, which can be deconvoluted into three sub-peaks at 284.9, 285.7, and 289.0 eV. These sub-peaks correspond to carbon atoms in C–C/C=C, C–N, and C–O bonds, respectively.[29,34] The O 1s spectrum, shown in Fig. 3c, displays two peaks at 532.2 and 533.7 eV, corresponding to C–O and C=O bonds, respectively. The high-resolution N 1s spectrum (Fig. 3d) shows a principal peak at 399.3 eV, indicating that most nitrogen atoms in PANi exist in the aniline form (–NH–). The presence of positively charged nitrogen atoms (N^+) can further improve the material's conductivity. Quinone imine (–NH^+=) and aniline (–NH–) can act as electron acceptors and donors, respectively, enhancing electron conductivity and providing additional charge storage sites.[35] Furthermore, Fig. S2† illustrates the Ti 2p spectrum, where the observed peaks at energies of 463.7 eV, 461.5 eV, 459.9 eV, 457.8 eV, and 454.9 eV can be assigned to Ti–O, Ti^{2+}, Ti–C, Ti^{3+}, and Ti–C species, respectively.[36,37]

3.3 Electrochemical performance analysis

The electrochemical performance of the prepared samples is presented in Fig. 4. The cyclic voltammetry (CV) curves of MXene, PANi, MX/PA, and CDP-MX/PA electrodes are shown in Fig. 4a, with a scan rate of 50 mV s^{-1}. MXene exhibits the smallest voltage window compared to other materials, and its

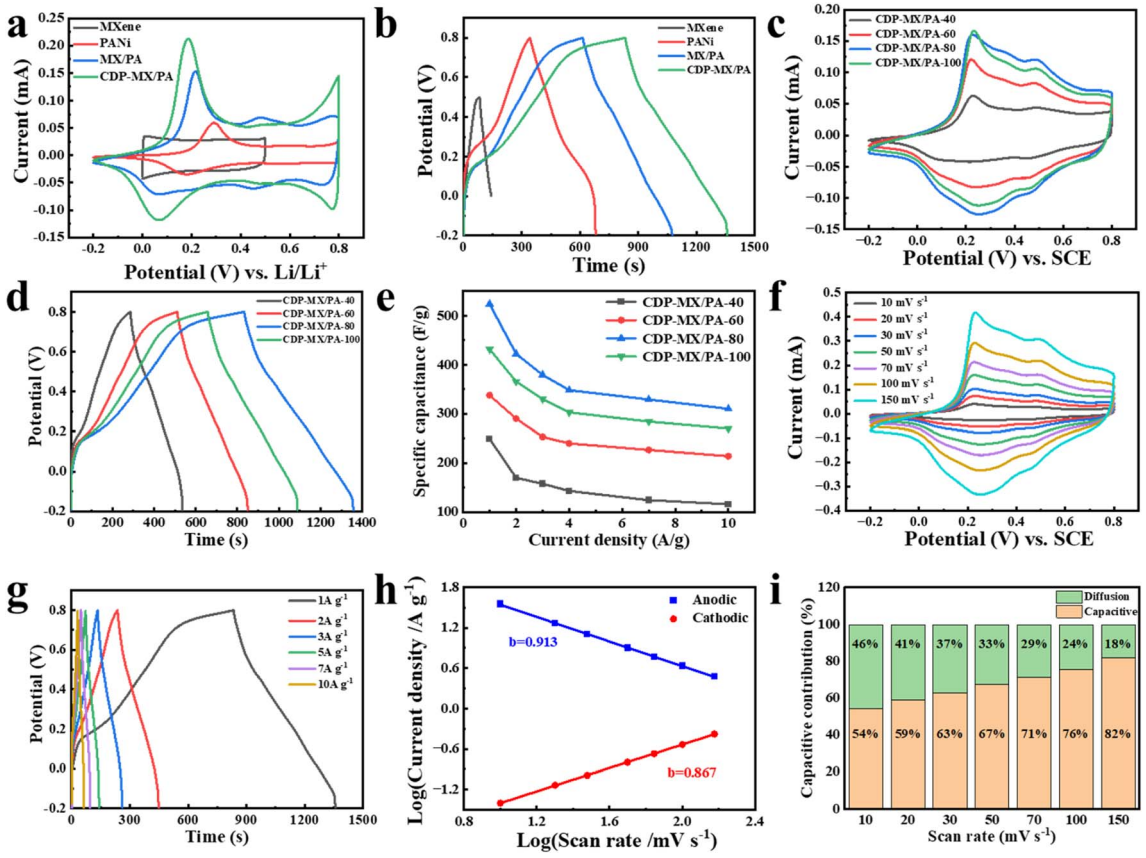

Fig. 4 (a) CV of MXene, PANi, MX/PA and CDP-MX/PA at a scanning speed of 50 mV s^{-1}; (b) GCD of MXene, PANi, MX/PA and CDP-MX/PA at a current density of 1 A g^{-1}; (c) CV of CDP-MX/PA-40, CDP-MX/PA-60, CDP-MX/PA-80 and CDP-MX/PA-100 at a scanning speed of 50 mV s^{-1}; (d) GCD of CDP-MX/PA-40, CDP-MX/PA-60, CDP-MX/PA-80 and CDP-MX/PA-100 at a current density of 1 A g^{-1}; (e) specific capacitance of CDP-MX/PA-40, CDP-MX/PA-60, CDP-MX/PA-80 and CDP-MX/PA-100 at different current densities. (f) CV of CDP-MX/PA-80 at scanning speeds of 10–150 mV s^{-1}; (g) GCD of CDP-MX/PA-80 at current densities of 1–10 A g^{-1}; (h) logarithmic relationship of peak current intensity and scan rate; (i) capacitive contributions of CDP-MX/PA-80 at different scan rates.

© 2024 The Author(s). Published by the Royal Society of Chemistry

Open Access Article. Published on 25 April 2024. Downloaded on 2/12/2026 9:24:58 AM. This article is licensed under a Creative Commons Attribution-NonCommercial 3.0 Unported Licence.

Table 1 Comparison of the specific capacitance of related materials

Sample	Specific capacitance (F g^{-1})	Potential range (V)	Electrolyte	Current density (A g^{-1})
MXene	118.8	0–0.5	1 M H_2SO_4	1.0
PANi	338.0	−0.2–0.8	1 M H_2SO_4	1.0
MX/PA-20	189.2	−0.2–0.8	1 M H_2SO_4	1.0
MX/PA-40	260.0	−0.2–0.8	1 M H_2SO_4	1.0
MX/PA-60	300.6	−0.2–0.8	1 M H_2SO_4	1.0
MX/PA-80	460.8	−0.2–0.8	1 M H_2SO_4	1.0
MX/PA-100	307.2	−0.2–0.8	1 M H_2SO_4	1.0
CDP-MX/PA-40	249.2	−0.2–0.8	1 M H_2SO_4	1.0
CDP-MX/PA-60	337.8	−0.2–0.8	1 M H_2SO_4	1.0
CDP-MX/PA-80	523.8	−0.2–0.8	1 M H_2SO_4	1.0
CDP-MX/PA-100	431.6	−0.2–0.8	1 M H_2SO_4	1.0

CV curve approaches a rectangular shape, indicating the characteristic of high reversibility in the double-layer capacitor (EDLC).[38] Compared to PANi, MXene, and MX/PA, the cyclic voltammetry (CV) curve of CDP-MX/PA exhibits higher peak currents, indicating that this composite has a higher specific capacitance. Furthermore, the CV curve of CDP-MX/PA displays the largest area, indicating its excellent capacitive behavior. The CV curve of CDP-MX/PA composite material shows a pair of redox peaks at 0.18 and 0.28 V relevant to the transition between the oxidized and reduced states of PANi in the composite.[39] Fig. 4b shows the constant current charge/discharge (GCD) curves of MXene, PANi, MX/PA, and CDP-MX/PA. It is evident that the discharge time of CDP-MX/PA is significantly longer than those of other materials, consistent with the CV results. As shown in Table 1, the specific capacitance of CDP-MX/PA composite material at 1 A g^{-1} is measured to be 523.8 F g^{-1}, much higher than that of MXene (118.8 F g^{-1}), PANi (338.0 F g^{-1}), and MX/PA (460.8 F g^{-1}). This is attributed to the presence of CDP on the surface of MXene suppresses the aggregation of PANi, inducing the polymerization of PANi monomers on the MXene surface, thus promoting synergistic interactions between different components.[16]

Fig. 4c displays the cyclic voltammetry (CV) curves of CDP-PA/MX prepared at different aniline concentrations (40–100 mM) at a scan rate of 50 mV s^{-1}. Oxidation and reduction peaks corresponding to PANi can be observed, indicating that PANi is the primary contributor to pseudocapacitance. Additionally, the CDP-MX/PA-80 composite material exhibits the largest enclosed area, suggesting that it has the highest capacitance. Fig. 4d illustrates the galvanostatic charge/discharge (GCD) curves of CDP-PA/MX prepared at different aniline concentrations (40–100 mM) at 1 A g^{-1}, with CDP-MX/PA-80 showing significantly longer discharge time compared to other materials. The capacitance retention of CDP-MX/PA materials prepared with different aniline concentrations (40–100 mM) at various current densities (1–10 A g^{-1}) was calculated, and the rate performance was compared, as shown in Fig. 4e. At 1.0 A g^{-1}, when the aniline concentration increased from 40 to 80 mM, the specific capacitance (C_s) of CDP-MX/PA increased from 249.2 to 523.8 F g^{-1}. However, at the highest concentration (100 mM), due to excessive aniline aggregation, disordered and interconnected PANi nanowires also appeared, leading to a decrease in Cs to 431.6 F g^{-1} for CDP-MX/PA. These results are consistent with the observed capacitance performance in the CV curves. As the scan rate increases, as shown in Fig. 4f, the oxidation peak shifts positively, the reduction peak shifts negatively, and the CV curves do not exhibit significant distortion, indicating that the capacitance of the CDP-MX/PA-80 composite material is a combination of double-layer capacitance and pseudocapacitance. The CV curves of CDP-MX/PA-40, CDP-MX/PA-60, and CDP-MX/PA-100 at different scan rates are presented in Fig. S3a–c.† It can be observed that the CV curves of CDP-MX/PA do not undergo severe deformation even at high scan rates. Fig. 4g illustrates the galvanostatic charge/discharge (GCD) curves of CDP-MX/PA-80 at various current densities, displaying good symmetry, indicating excellent reversibility in the capacitive behavior. The galvanostatic charge/discharge (GCD) curves of the composite materials prepared with different aniline concentrations (40–100 mM) are shown in Fig. S3d–f.† With increasing aniline concentration, the specific capacitance of the CDP-MX/PA composite material initially increases and then decreases. When the concentration of aniline monomers exceeds 80 mM, excessive aniline monomers undergo polymerization and subsequent aggregation, hindering the penetration of ions through the active material and resulting in a decrease in the capacitance of the composite material. For the CDP-MX/PA-80 composite material, the fitted slopes (b value) are 0.913 and 0.867, indicating a mixed charge storage mechanism involving both diffusion control and capacitance processes (Fig. 4h).[40,41] As the scan rate increases from 10 mV s^{-1} to 150 mV s^{-1}, the capacitance contribution of CDP-MX/PA-80 gradually rises from 54.2% to 81.8% (Fig. 4i). This indicates that with the increase in scan rate, the pseudo-capacitive effect of the material enhances, implying a more effective charge storage capability. This enhancement is likely attributed to the increased migration speed of charges at higher scan rates, enabling more charges to be stored and released within a unit of time, thereby elevating the material's capacitance contribution.[16,42,43]

The separated cyclic voltammetry (CV) curves between total current and capacitive current for CDP-MX/PA-80 at different scan rates are illustrated in Fig. S4.† CV curves for MXene and

 © 2024 The Author(s). Published by the Royal Society of Chemistry

Open Access Article. Published on 25 April 2024. Downloaded on 2/12/2026 9:24:58 AM.
This article is licensed under a Creative Commons Attribution-NonCommercial 3.0 Unported Licence.

PANi at various scan rates and galvanostatic charge/discharge (GCD) curves at different current densities are presented in Fig. S5.† CV and GCD curves for MX/PA-20, MX/PA-40, MX/PA-60, MX/PA-80, and MX/PA-100 at different scan rates and current densities are depicted in Fig. S6 and S7.† Combining the equations, Table 1 is derived, clearly indicating that the overall performance of CDP-MX/PA composite materials surpasses that of MX/PA composites.

Electrochemical Impedance Spectroscopy (EIS) is an essential technique for studying the electrochemical properties of the tested electrodes. Fig. S8† depicts the Nyquist plots of PANI, MX/PA, and CDP-MX/PA (frequency range: 10 kHz to 0.01 Hz), with an inset showing the high-frequency magnified region. A typical Nyquist plot consists of semicircular arcs and sloping lines in the high and low-frequency regions, respectively. In the high-frequency region, the diameter of the semicircular arc corresponds to the charge transfer resistance (R_{ct}), while the intercept with the real axis represents the equivalent series resistance (R_s).[44] R_{ct} is a crucial parameter for determining the electrochemical performance of the working electrode, associated with the charge transfer at the electrode/electrolyte interface.[45] Clearly, the smaller diameter of the semicircle for CDP-MX/PA-80 implies that the R_{ct} of the CDP-MX/PA-80 electrode is smaller than that of the other five electrodes, indicating good charge transfer at the electrode/electrolyte interface. From the graph, it can also be inferred that the equivalent series resistances (R_s) of several materials are low, indicating fast electron transport speeds. Additionally, the R_{ct} of the MX/PA composite material is lower than that of pure PANI. The porous structure formed by PANI nanowires provides channels for the entry of electrolyte ions and reduces the charge transfer impedance of the MX/PA composite material.[46] The high electrochemical activity of PANI and the high electrical conductivity of MXene collectively enhance the electrochemical performance of the MX/PA composite material. With the addition of CDP, the synergistic effect among the three further reduces the material's R_{ct}. These results indicate that CDP-MX/PA composite materials exhibit higher electrochemical activity and faster reaction kinetics.

CDP-MX/PA-80 was employed as an electrode material for constructing a symmetrical supercapacitor. Fig. 5a displays the cyclic voltammetry (CV) curves of the device across various voltage windows at a scan rate of 50 mV s^{-1}. These curves show a quasi-rectangular shape, indicating a potential voltage window up to 1.4 V. Beyond this, polarization is observed with a slight current transition, suggesting the limit of the operable voltage window is 0–1.4 V. Fig. 5b illustrates the CV curves of the CDP-MX/PA-80||CDP-MX/PA-80 device within a 0–1.4 V window at different scan rates, revealing typical redox behavior indicative of pseudocapacitive supercapacitors. Notably, even at

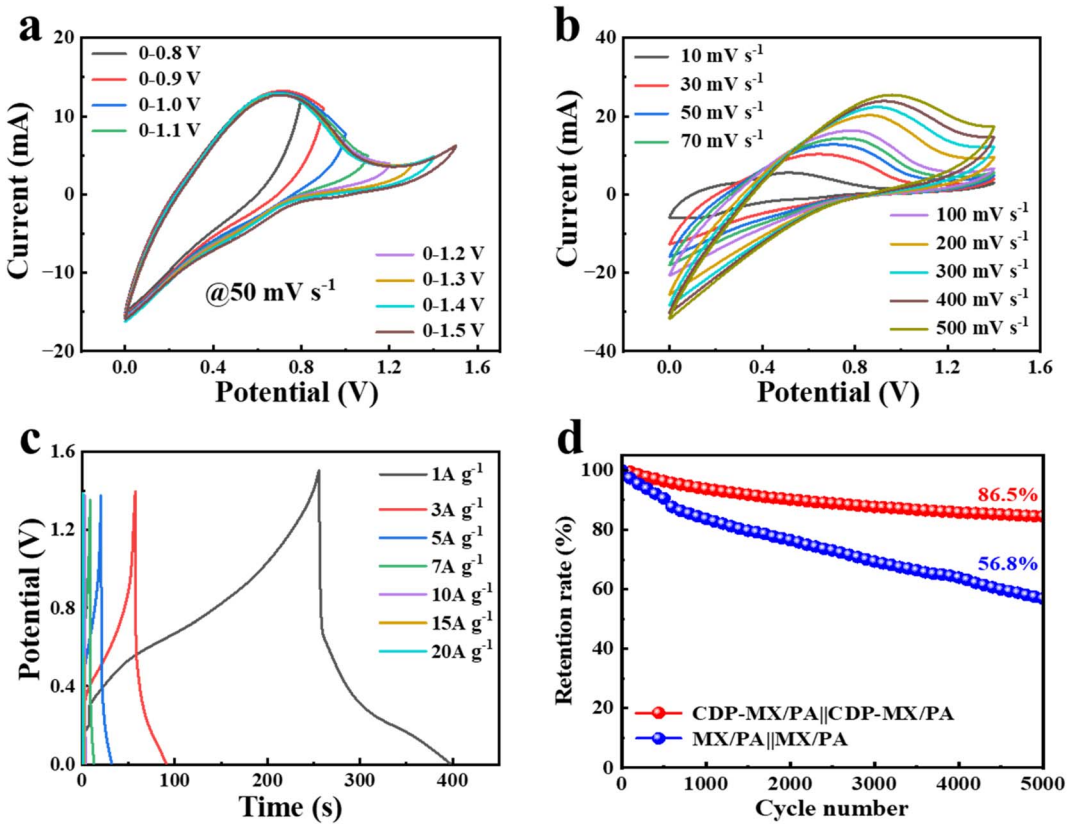

Fig. 5 (a) and (b) CV curves of CDP-MX/PA||CDP-MX/PA supercapacitor at different potential windows and different scan rates, respectively; (c) GCD curves of CDP-MX/PA||CDP-MX/PA supercapacitor at different current densities, respectively; (d) cycling stability of CDP-MX/PA||CDP-MX/PA device and MX/PA||MX/PA device.

Open Access Article. Published on 25 April 2024. Downloaded on 2/12/2026 9:24:58 AM. This article is licensed under a Creative Commons Attribution-NonCommercial 3.0 Unported Licence.

elevated scan rates up to 500 mV s^{-1}, the CV curves retain their integrity without significant distortion, affirming the device's excellent rate performance. Furthermore, at a current density of 1 A g^{-1}, the device demonstrates a high specific capacitance of 101.6 F g^{-1}, underscoring its remarkable mass-specific capacitance. Remarkably, even at an increased current density of 20 A g^{-1}, the CDP-MX/PA-80 shows enhanced voltage window and rate performance post CDP-assisted polymerization, in contrast to the MX/PA-80‖MX/PA-80 (referenced in Fig. S9†). The endurance test over 5000 cycles at 5 A g^{-1} reveals that CDP-MX/PA-80 retains 86.5% of its initial specific capacitance, significantly outperforming MX/PA-80, which maintains only 56.8% of its capacitance, thereby highlighting the superior cyclic stability of CDP-MX/PA-80. This is because during repeated charge–discharge cycles, polyaniline (PANI) experiences issues such as deprotonation and expansion/contraction, leading to a gradual reduction in its capacity. Although incorporating PANI molecular chains onto CDP-modified MXene significantly mitigates the deprotonation issue, it fails to buffer the structural stress caused by expansion/contraction. While combining the two-dimensional material with PANI effectively alleviates the expansion/contraction problem, it cannot maintain the PANI framework under locally high acidity conditions to suppress deprotonation. Therefore, the modified CDP-MX/PA cathode will ultimately experience noticeable capacity loss.

Fig. S10† elucidates the changes in equivalent series resistance (ESR) of the CDP-MX/PA-80‖CDP-MX/PA-80 device before and after extensive cycling. The increase in internal and charge transfer resistance post-cycling suggests a notable impact of ion insertion on the material's resistance properties. Power density and energy density are indispensable parameters for evaluating the electrochemical performance of supercapacitors. As shown in Fig. S11,† the CDP-MX/PA-80 device can deliver a high energy density of 27.7 W h kg^{-1} at a power density of 700 W kg^{-1}.

4 Conclusion

The CDP assisted in the growth of PANi represented an efficient and environmentally friendly synthesis method for supercapacitor electrode material. To address the issue of reduced electrochemical performance caused by the stacking of 2D materials,[47] we have adopted the following strategies: (1) surface functionalization: surface functionalization of MXene with CDP improves the protonation degree of PANI. This process aids in continuous proton provision and maintains local high acidity, thus suppressing its chronic deprotonation, thereby enhancing the oxidation-reduction activity and reversibility of PANI. (2) Enhancing conductivity and flexibility: MXene possesses excellent conductivity and flexibility, facilitating the rapid oxidation–reduction reactions of PANI and buffering its corresponding expansion/contraction. The combination of these methods can ameliorate the stacking issues of 2D materials as electrode materials for supercapacitors and improve their electrochemical performance. The specific capacitance of CDP-MX/PA is 523.8 F g^{-1}. Compared to MXene, the specific capacitance has increased by 4.5 times and 1.5 times respectively. The CDP-MX/PA-based symmetrical supercapacitor deliver a high energy density of 27.7 W h kg^{-1} and a stable cycle lifespan with 86.5% capacity retention after 5000 cycles. Utilizing CDP-functionalized MXene as the template for PANi polymerization offers several advantages, including (1) reducing the disorderly aggregation of PANi, (2) increasing the contact area between electrolyte ions and the material to maintain efficient ion transport, and (3) limiting the expansion and contraction of the PANi framework to enhance its cyclic stability. Consequently, the CDP-MX/PA composite material holds significant promise for widespread applications in energy storage devices, particularly supercapacitors.

Conflicts of interest

There are no conflicts to declare.

Acknowledgements

This work was supported by the National Natural Science Foundation of China (No. 21703200 and 21773203), the Basic Science Research Program through the National Research Foundation of Korea (NRF) funded by the Ministry of Education (NRF-2022R1A6A1A03063039), and the Natural Science Foundation of Jiangsu Province of China (BX2023026).

References

1 Y. Zhang, Z. Song, L. Miao, Y. Lv, L. Gan and M. Liu, *ACS Appl. Mater. Interfaces*, 2023, **15**, 35380–35390.
2 C. Hu, Y. Qin, Z. Song, P. Liu, L. Miao, H. Duan, Y. Lv, L. Xie, M. Liu and L. Gan, *J. Colloid Interface Sci.*, 2024, **658**, 856–864.
3 M. Mansuer, L. Miao, Y. Qin, Z. Song, D. Zhu, H. Duan, Y. Lv, L. Li, M. Liu and L. Gan, *Chin. Chem. Lett.*, 2023, **34**, 107304.
4 K. S. Poonam, A. Arora and S. K. Tripathi, *J. Energy Storage*, 2019, **21**, 801–825.
5 T. Xu, Y. X. Wang, K. Liu, Q. S. Zhao, Q. D. Liang, M. Zhang and C. L. Si, *Adv. Compos. Hybrid Mater.*, 2023, **6**, 108.
6 Z. M. Fan, Y. S. Wang, Z. M. Xie, D. L. Wang, Y. Yuan, H. J. Kang, B. L. Su, Z. J. Cheng and Y. Y. Liu, *Adv. Sci.*, 2018, **5**, 1800750.
7 S. S. Zheng, H. J. Zhou, H. G. Xue, P. Braunstein and H. Pang, *J. Colloid Interface Sci.*, 2022, **614**, 130–137.
8 L. Jia, S. Q. Zhou, A. Ahmed, Z. C. Yang, S. Q. Liu, H. Wang, F. Li, M. Zhang, Y. J. Zhang and L. Y. Sun, *Chem. Eng. J.*, 2023, **475**, 146361.
9 T. Shimada, N. Takenaka, Y. Ando, M. Otani, M. Okubo and A. Yamada, *Chem. Mater.*, 2022, **34**, 2069–2075.
10 Y. Q. Zhu, H. Xu, P. D. Chen, Y. H. Bao, X. D. Jiang and Y. Chen, *Electrochim. Acta*, 2022, **413**, 140146.
11 A. Eftekhari, L. Li and Y. Yang, *J. Power Sources*, 2017, **347**, 86–107.
12 W. L. Luo, Y. D. Wei, Z. Zhuang, Z. T. Lin, X. Li, C. P. Hou, T. X. Li and Y. Ma, *Electrochim. Acta*, 2022, **406**, 139871.
13 Y. D. Wei, W. L. Luo, X. Li, Z. T. Lin, C. P. Hou, M. L. Ma, J. X. Ding, T. X. Li and Y. Ma, *Electrochim. Acta*, 2022, **406**, 139874.

© 2024 The Author(s). Published by the Royal Society of Chemistry

Open Access Article. Published on 25 April 2024. Downloaded on 2/12/2026 9:24:58 AM. This article is licensed under a Creative Commons Attribution-NonCommercial 3.0 Unported Licence.

14 W. Zhang, X. Jin, H. Chai, G. Diao and Y. Piao, *Adv. Mater. Interfaces*, 2018, **5**, 1800106.
15 W. Zhang, Z. Zheng, L. Lin, X. Zhang, M. Bae, J. Lee, J. Xie, G. Diao, H. J. Im, Y. Piao and H. Pang, *Adv. Sci.*, 2023, **10**, 2304062.
16 W. Zhang, J. Guo, T. Chen, S. Park, M. Bae, Y. Cho, G. Diao, L. Lin and Y. Piao, *Mater. Today Chem.*, 2023, **33**, 101733.
17 J. J. Jiang, X. Y. Lin and G. W. Diao, *ACS Appl. Mater. Interfaces*, 2017, **9**, 36688–36694.
18 N. Cheng, Y. Chen, J. Yu, J. J. Li and Y. Liu, *ACS Appl. Mater. Interfaces*, 2018, **10**, 6810–6814.
19 A. Galan and P. Ballester, *Chem. Soc. Rev.*, 2016, **45**, 1720–1737.
20 Y. Huang, Q. Lu, D. Wu, Y. Jiang, Z. Liu, B. Chen, M. Zhu and O. G. Schmidt, *Carbon Energy*, 2022, **4**, 598–620.
21 Y. Liu, Z. Dai, W. Zhang, Y. Jiang, J. Peng, D. Wu, B. Chen, W. Wei, X. Chen, Z. Liu, Z. Wang, F. Han, D. Ding, L. Wang, L. Li, Y. Yang and Y. Huang, *ACS Nano*, 2021, **15**, 9065–9075.
22 C. L. Liu, Y. Bai, W. T. Li, F. Y. Yang, G. X. Zhang and H. Pang, *Angew. Chem., Int. Ed.*, 2022, **61**, e2021162.
23 W. Zhang, L. W. Lin, J. Q. Guo, M. Wu, S. Park, H. Yao, S. H. Paek, G. W. Diao and Y. Piao, *Research*, 2022, 9814638.
24 J. J. Xu, K. Wang, S. Z. Zu, B. H. Han and Z. X. Wei, *ACS Nano*, 2010, **4**, 5019–5026.
25 H. Xu, D. Zheng, F. Liu, W. Li and J. Lin, *J. Mater. Chem. A*, 2020, **8**, 5853–5858.
26 A. Prasannan, L. B. T. Tram, P. D. Hong, N. Somanathan, I. Shown and T. Imae, *Langmuir*, 2011, **27**, 766–773.
27 S. Y. Li, A. M. Gao, F. Y. Yi, D. Shu, H. H. Cheng, X. P. Zhou, C. He, D. P. Zeng and F. Zhang, *Electrochim. Acta*, 2019, **297**, 1094–1103.
28 Z. C. Yang, Y. Zhang, J. H. Kong, S. Y. Wong, X. Li and J. Wang, *Chem. Mater.*, 2013, **25**, 704–710.
29 L. Lyu, H. Chai, K. D. Seong, C. Lee, J. Kang, W. Zhang and Y. Piao, *Electrochim. Acta*, 2018, **291**, 256–266.
30 K. Kannan, M. H. Sliem, A. M. Abdullah, K. K. Sadasivuni and B. Kumar, *Catalysts*, 2020, **10**, 549.
31 W. Zhang, X. D. Gong, Y. Cai, C. L. Zhang, X. Yu, J. Fan and G. W. Diao, *Carbohydr. Polym.*, 2013, **95**, 366–370.
32 W. Zhang, X. D. Gong, C. Liu, Y. Z. Piao, Y. Sun and G. W. Diao, *J. Mater. Chem. B*, 2014, **2**, 5107–5115.
33 Y. H. Wang, X. Chu, Z. H. Zhu, D. Xiong, H. T. Zhang and W. Q. Yang, *Chem. Eng. J.*, 2021, **423**, 130203.
34 F. Guo, J. Q. Guo, Z. Q. Zheng, T. Xia, A. N. Chishti, L. W. Lin, W. Zhang and G. W. Diao, *Chin. Chem. Lett.*, 2022, **33**, 4846–4849.
35 J. G. Dai, X. H. Wang, L. Xia, L. L. Luo, D. X. Li, C. Y. Yang, Y. T. Xu and L. Z. Dai, *J. Energy Storage*, 2022, **55**, 105436.
36 S. Wei, J. Ma, D. Wu, B. Chen, C. Du, L. Liang, Y. Huang, Z. Li, F. Rao, G. Chen and Z. Liu, *Adv. Funct. Mater.*, 2023, **33**, 2209806.
37 W. Xu, L.-H. Wang, Y. Chen and Y. Liu, *Mater. Today Chem.*, 2022, **24**, 100896.
38 A. Patra, P. Mane, S. R. Polaki, B. Chakraborty and C. S. Rout, *J. Energy Storage*, 2022, **54**, 105355.
39 K. P. Gautam, D. Acharya, I. Bhatta, V. Subedi, M. Das, S. Neupane, J. Kunwar, K. Chhetri and A. P. Yadav, *Inorganics*, 2022, **10**, 86.
40 Y. Bai, C. L. Liu, T. T. Chen, W. T. Li, S. S. Zheng, Y. C. Pi, Y. S. Luo and H. Pang, *Angew. Chem., Int. Ed.*, 2021, **60**, 25318–25322.
41 F. Yu, Z. C. Liu, R. W. Zhou, D. M. Tan, H. X. Wang and F. X. Wang, *Mater. Horiz.*, 2018, **5**, 529–535.
42 X. J. Pu, D. Zhao, C. L. Fu, Z. X. Chen, S. N. Cao, C. S. Wang and Y. L. Cao, *Angew. Chem., Int. Ed.*, 2021, **60**, 21310–21318.
43 L. Sang, M.-l. Wang and d. Huang Cheng, *Chin. J. Power Sources*, 2007, **31**, 697–700.
44 J. Wang, X. Luo, C. Young, J. Kim, Y. V. Kaneti, J. You, Y.-M. Kang, Y. Yamauchi and K. C. W. Wu, *Chem. Mater.*, 2018, **30**, 4401–4408.
45 J. Li, X. Yuan, C. Lin, Y. Yang, L. Xu, X. Du, J. Xie, J. Lin and J. Sun, *Adv. Energy Mater.*, 2017, **7**, 1602725.
46 Y. Qiu, M. Hou, J. Gao, H. Zhai, H. Liu, M. Jin, X. Liu and L. Lai, *Small*, 2019, **15**, 1903836.
47 Y. Huang, M. Zhu, W. Meng, Y. Fu, Z. Wang, Y. Huang, Z. Pei and C. Zhi, *RSC Adv.*, 2015, **5**, 33981–33989.

© 2024 The Author(s). Published by the Royal Society of Chemistry